ASME Journal of Applied Mechanics
Online journal at:
https://asmedigitalcollection.asme.org/appliedmechanics

Lianchao Wang
National Key Laboratory of Science and Technology on Advanced Composites in Special Environments, Harbin Institute of Technology, Harbin 150001, China;
Université de Franche-Comté, CNRS, Institut FEMTO-ST, Besançon 25000, France;
Department of Mechanical Engineering, City University of Hong Kong, Hong Kong SAR, China
e-mail: lianchaowang@outllook.com

Julio A. Iglesias Martínez
Université de Franche-Comté, CNRS, Institut FEMTO-ST, Besançon 25000, France
e-mail:joulesiglesias@gmail.com

Krzysztof K. Dudek
Université de Franche-Comté, CNRS, Institut FEMTO-ST, Besançon 25000, France;
Institute of Physics, University of Zielona Gora, ul. Szafrana 4a, Zielona Gora 65-069, Poland
e-mail: K.Dudek@if.uz.zgora.pl

Gwenn Ulliac
Université de Franche-Comté, CNRS, Institut FEMTO-ST, Besançon 25000, France
e-mail: gwenn.ulliac@femto-st.fr

Xinrui Niu
Department of Mechanical Engineering, City University of Hong Kong, Hong Kong SAR 999077, China
e-mail: xinrui.niu@cityu.edu.hk

Yajun Zou
National Key Laboratory of Science and Technology on Advanced Composites in Special Environments, Harbin Institute of Technology, Harbin 150001, China
e-mail: zouyajun95@163.com

Multistep and Elastically Stable Mechanical Metamaterials

Materials and structures with tunable mechanical properties are essential for numerous applications. However, constructing such structures poses a great challenge since it is normally very complicated to change the properties of a material after its fabrication, particularly in pure force fields. Herein, we propose a multistep and elastically stable 3D mechanical metamaterial having simultaneously tunable effective Young's modulus and auxeticity controlled by the applied compressive strain. Metamaterial samples are fabricated by 3D printing at the centimetric scale, with selective laser sintering, and at the micrometric scale, with two-photon lithography. Experimental results indicate an elementary auxeticity for small compressive strains but superior auxeticity for large strains. Significantly, the effective Young's modulus follows a parallel trend, becoming larger with increasing compressive strain. A theoretical model explains the variations of the elastic constants of the proposed metamaterials as a function of geometry parameters and provides a basic explanation for the appearance of the multistep behavior. Furthermore, simulation results demonstrate that the proposed metamaterial has the potential for designing metamaterials exhibiting tunable phononic band gaps. The design of reusable elastically stable multistep metamaterials, with tunable mechanical performances supporting large compression, is made possible thanks to their delocalized deformation mode.
[DOI: 10.1115/1.4066084]

Keywords: constitutive modeling of materials, mechanical properties of materials, structures, wave propagation

[1]Corresponding authors.
Contributed by the Applied Mechanics Division of ASME for publication in the Journal of Applied Mechanics. Manuscript received May 31, 2024; final manuscript received July 22, 2024; published online August 21, 2024. Assoc. Tech: Pradeep Sharma.

Bing Wang[1]
National Key Laboratory of Science
and Technology on Advanced Composites
in Special Environments,
Harbin Institute of Technology,
Harbin 150001, China
e-mail: wangbing86@hit.edu.cn

Vincent Laude[1]
Université de Franche-Comté,
CNRS, Institut FEMTO-ST,
Besançon 25000, France
e-mail: vincent.laude@femto-st.fr

Muamer Kadic[1]
Université de Franche-Comté,
CNRS, Institut FEMTO-ST,
Besançon 25000, France
e-mail: muamer.kadic@univ-fcomte.fr

1 Introduction

Over the last decade, metamaterials have been rising exponentially [1–5], and even more so for mechanical metamaterials [6–27] thanks to new fabrication techniques such as 3D printing [28–34]. Generally, after the manufacturing process, the mechanical behavior of a metamaterial is set and is hardly modified [35–37]. Nevertheless, materials and structures with varying static or dynamical mechanical properties are attractive to many engineering fields [7,35,38–43]. To implement them, numerous methods have been proposed and many metamaterials and metastructures with tunable mechanical behaviors have been investigated. For instance, Janbaz et al. [38] proposed a bi-beam that consists of two beams with different viscoelasticity to design metamaterials with strain-rate-dependent mechanical behavior. Liang et al. [44] used magnetic interactions to change globally the energy and thus the configuration of a system. Mü et al. [42] investigated a metamaterial with different auxeticities under varying optical stimuli. Ji et al. [45] used a bi-material beam showing varying mechanical response as a function of temperature for soft microrobotic applications. Farzaneh et al. [46] proposed a sequential metamaterial with alternating Poisson's ratios. Dudek et al. [47] used magnetic inclusions to reconfigure a structure and tune the mechanical performance of the entire system. Wang et al. [48] demonstrated a metamaterial that exhibits a change in the sign of the effective tangent Poisson's ratio during compression, without significant enhancement in Young's modulus.

There are three main principles to design metamaterials with tunable mechanical properties, i.e., the principle of structural instabilities and material postbuckling [49,50], the use of multibody systems [39,51,52], and the theory of multimaterial systems [42,47]. In principle, these methods are efficient for obtaining metamaterials with tunable mechanical behaviors. Nevertheless, some additional limitations are introduced, for instance, global elastic instabilities of the whole system, excess challenges for fabrication technology, demanding requirements for multiphysical fields, etc. Furthermore, most previous studies have focused on a single adjustable mechanical property [48], implying that the adjustability of other mechanical parameters of the metamaterial has been ignored or sacrificed. Indeed, materials with several tunable mechanical parameters in different states can introduce multiple functionalities.

As two fundamental and significant mechanical properties of materials, Young's modulus and Poisson's ratio (in particular, if the latter value is negative, i.e., for auxeticity) play essential roles in material investigations and applications [6,36,39,43,53–55]. Mechanical metamaterials with simultaneously tunable Young's modulus and auxeticity have rarely been reported but are highly desirable and offer a significant commercial appeal. For instance, in the case of applications requiring the tunable load-bearing capacity and volume change at the same time, it is essential to harness the ability to design materials with both of these mechanical properties being adjustable. In this regard, we consider in this work a single constituent material to design a mechanical metamaterial that shows elastically stable adjustable elastic constants under variable compressive strain. First, the geometry configuration and samples of the proposed metamaterial are designed and fabricated at the centimetric and micrometric scales. Then, a theoretical model of the effective elastic constants is built to reveal the effects of geometrical parameters and to explain the multistep behavior of the metamaterial. The tunable Young's modulus and auxeticity in different steps are discussed experimentally. In addition, the potential application to metamaterials with adjustable phononic band gaps is investigated numerically. Finally, the delocalized deformation mode and the reusable properties of the metamaterials are revealed.

2 Structural Design

In a previous work [56], inspired by the shape of latitude and longitude lines around the earth, some of us proposed and investigated a primitive motif substructure that exhibits nonauxeticity in the x direction but auxeticity in the y direction when either compression or stretching is applied along the z direction, as depicted in Fig. 1(*a*). This partially auxetic substructure consists of two different elliptical rings located in perpendicular planes, that is, in the xy plane and the xz plane.

Herein, we set the geometry dimensions of the substructure in the x, y, and z directions as $2a$, $2a/m$, and $2a/n$, respectively. The geometry parameters m and n are dimensionless and independent of each other, which are used to describe the shape of the elliptical ring in the xy plane and the xz plane. It is clear that m or n equals 1 means that the ring is circular, otherwise, it is elliptic. In addition, all elliptical rings of the substructure have identical cross sections, specifically the same width b and thickness t. Another significant geometry parameter is the distance between the outer surfaces of two adjacent elliptical rings in the xz plane, t_c. Parameter t_c has a crucial influence on the tunable effective elastic constants obtained at different compression steps and will be discussed in detail in the following sections.

The results in Ref. [56] demonstrate that the auxeticity of the substructure only depends on the geometry parameters m and n, which means that the lateral deformation characteristics of the considered metamaterial depend on the shape of these two orthogonal elliptical

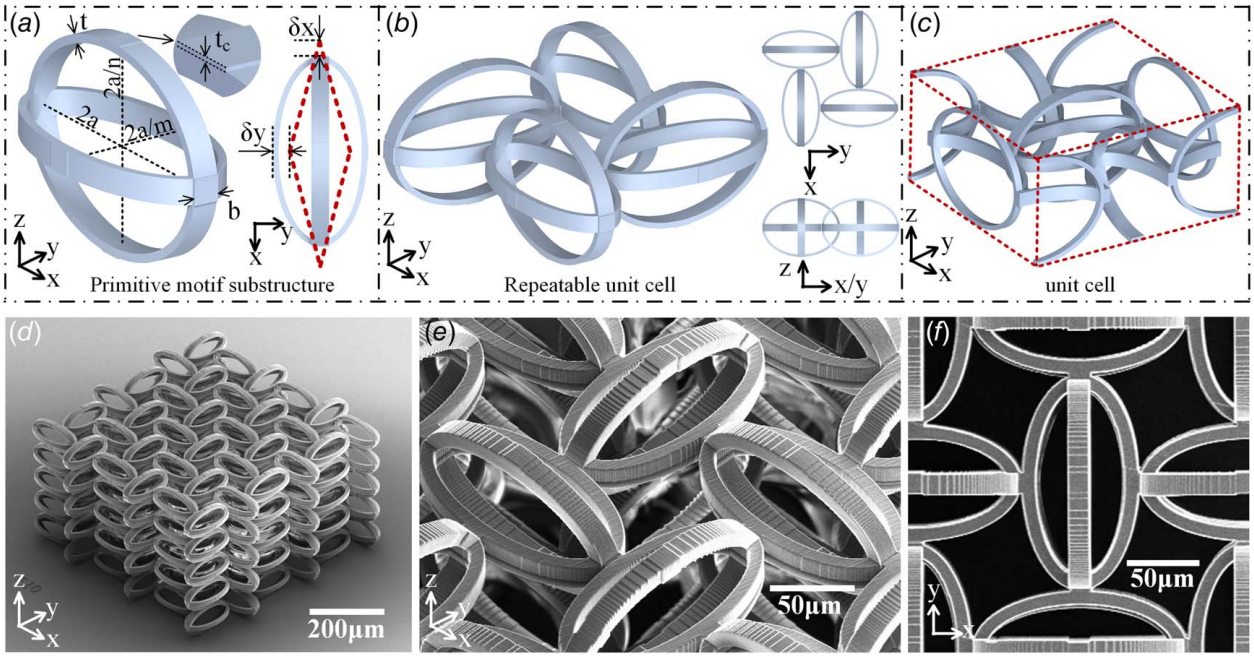

Fig. 1 Structure design of multistep mechanical metamaterials. (*a*) The primitive motif substructure shows auxeticity in the *y* and *z* directions but nonauxeticity in the *x* direction. It is worth noting that for some specific geometrical parameters, i.e., *m* and *n* (see the text for their definition), the contraction in the *y* direction surpasses the expansion in the *x* direction when compression is applied in the *z* direction, that is, $\delta y > \delta x$. (*b*) The repeatable unit cell with auxeticity in three principal directions is obtained by alternatively arranging the partially auxetic substructure in the *x* and *y* directions. (c) The primitive unit cell is used for phononic band structure computations. We use the repeatable unit cell for experiments, rather than the primitive unit cell because the former can diminish boundary effects when the number of unit cells composing the sample is limited. (*d–f*) SEM images of a sample composed of $3 \times 3 \times 5$ unit cells fabricated with two-photon lithography. Here, $m = n = 1.97$ with other parameters fixed as $a = 75\,\mu$m, $t = 10\,\mu$m, $b = 16\,\mu$m, and $t_c = 0.5\,\mu$m. (*d*) is an oblique view of the sample, whereas (e) and (*f*) show zoomed-in details of the sample.

rings. For some geometry parameters, significantly, an important property of this substructure is that shrinkage in the *y* direction is larger than expansion in the *x* direction if the compressive loading is applied from the *z* direction, that is, $\delta y > \delta x$, as shown with a dotted line in Fig. 1(*a*). It is worth noting that δx and δy denote the absolute deformations of the substructure rather than the corresponding effective strains. Based on this inherent property, four substructures can be arranged alternatively in the *x* and *y* directions to obtain a repeatable unit cell exhibiting auxeticity in all three orthogonal directions, as illustrated in Fig. 1(*b*). The corresponding primitive unit cell is depicted in Fig. 1(*c*).

As a note, there are three main differences between the original substructure in Fig. 1(*a*) and the new unit cell proposed in Fig. 1(*c*). First, the anisotropic properties of the two unit cells are different. The original substructure exhibits anisotropy in the three principal directions, whereas the new unit cell has identical mechanical properties in both *x* and *y* directions because of symmetry. Second, the original substructure is nonauxetic in one principal direction but auxetic in the other two principal directions. In contrast, the new unit cell is fully auxetic in all three principal directions. Third, elastically stable multistep mechanical behavior is hardly achieved by the original substructure, as it avoids self-contacts under large compression. The elastically stable multistep mechanical behavior resulting from self-contact is the distinctive property of the proposed metamaterial and is discussed in detail in this work.

3 Materials and Methods

3.1 Fabrication. A commercial 3D printer based on the principles of two-photon lithography 3D direct laser writing technology was used to prepare microscale metamaterials, as shown in Figs. 1(*d*)–1(*f*). The parent material for these samples is the customized commercial negative tone IP-S resin.

Young's modulus, Poisson's ratio, and density for the raw resin material are $E = 4$ GPa, $\nu = 0.3$, and $\rho = 1190\ \text{kg/m}^3$, respectively. For the Nanoscribe printing, the slicing distance and the hatching distance are prescribed to 1 μm and 0.5 μm, respectively.

A drop of IP-S resin was deposited on an indium tin oxide (ITO)-coated soda-lime glass substrate with dimensions 25 mm × 25 mm × 0.7 mm and photopolymerized with a femtosecond laser operating at $\lambda = 780$ nm and a 25× objective. The sample comprises $3 \times 3 \times 5$ unit cells (see Fig. 1(*d*)) in the main directions, and each repeatable unit cell (see Fig. 1(*b*)) was printed layer by layer from bottom to top. After printing, the samples were developed for 30 min in a propylene glycol methyl ether acetate solution to remove the unexposed photoresist and were rinsed for 5 min in isopropyl alcohol to clear the developer. Laser power at the level of 90% and a galvanometric scan speed of 100 mm/s were used for the whole fabrication process.

The centimetric samples (see Fig. 6(*a*)) were fabricated by a commercial 3D printing company with a selective laser sintering 3D printing craft. Thermoplastic urethane (TPU) with white color was used as the raw material. Young's modulus, Poisson's ratio, density, and the elongation of the raw material TPU are 27 MPa, 0.45, 1200 kg/m^3, and 500%, respectively.

3.2 Mechanical Tests. To evaluate the static mechanical properties of the metamaterials, quasi-static uniaxially compressive experiments were performed. Five samples were prepared at the microscale and were tested with a homemade setup with a load capacity of 5 N, a resolution of 10^{-6} N, and a compression speed set to 1 μm/s. At the same time, a microscope equipped with a lens of 20× magnification and a recording rate of 1 frame per second was used to capture the deformation of the sample in time. A video for the whole compressive process was exported. More specifically, the image tracking functions from MATLAB

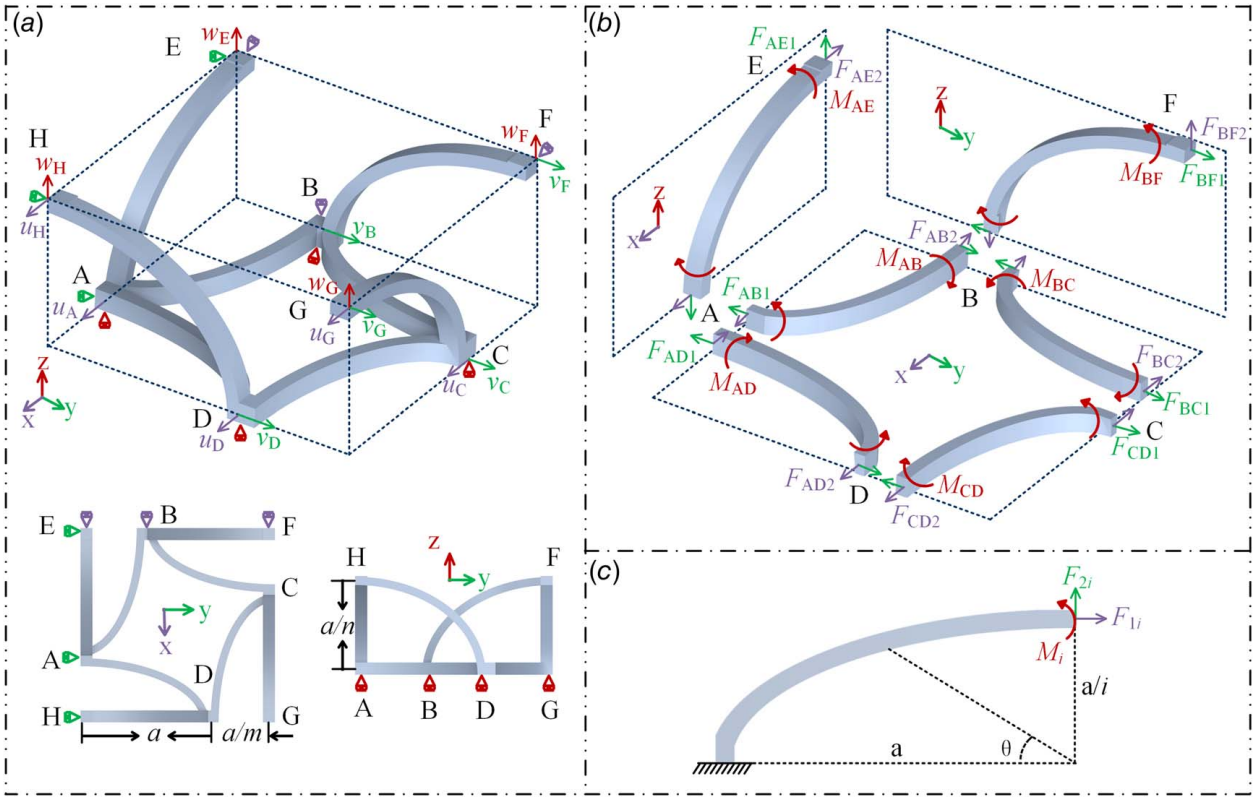

Fig. 2 Force analysis of mechanical metamaterials under loading in the *z* direction and periodic boundary conditions. (*a*) Force analysis of a 1/8th representative volume element of the proposed metamaterial, (*b*) decomposition of the 1/8th representative volume element, and (*c*) force analysis for each single beam.

software were employed to process and extract lateral deformations of the microscale samples. In terms of macroscopic testing, the five cycles of the loading and unloading experiments for each sample on a centimeter scale were implemented in an INSTRON 5569 mechanical tester with a load cell capacity of 50 kN. The compressive speed was fixed at 1 mm/s to maintain the quasi-static deformation and avoid dynamic effects. At the same time, commercial digital image correlation (DIC) equipment was used to record lateral deformations along the course. The applied DIC device measures arbitrary displacements down to nanometer resolution. Here, strain measurements from 50 microstrain to 2500% and above are available with 10–50 microstrain or better strain resolution. The device allows to assess specimen sizes ranging from 1 mm to 100 mm as well as to capture dynamic events at the rate of 5,000,000 frames per second. Images were processed by matching software VIC-3D, where a contour representing the displacement in the *x* direction was output directly, as shown in Fig. 6(*g*).

3.3 Analytical Model. To obtain the effective mechanical properties of the metamaterial, a theoretical model was built based on the force method of continuum mechanics. The following assumptions were made. First, we used the unit cell shown in Fig. 1(*c*) as the representative volume element for the metamaterial, and periodic boundary conditions were applied in all three principal directions. Second, the situation that the structure is under small compressive/stretch deformation in the *z* direction is taken into consideration merely. Then, all joints in the structure are assumed to be rigid. Moreover, the axial and shear deformations are neglected so it can be assumed that all members in the proposed structure are Euler beams that are deforming by bending only [57].

Herein, we assume that a stretch (or a compressive) predisplacement is applied in the *z* direction on the representative volume element. As declared above, it is clear that the mechanical properties of the structure in the *x* and *y* directions are identical. Due to the symmetry of the structure in the three principal directions, the loading and corresponding boundary conditions of a 1/8th representative volume element are considered and analyzed, as shown in Fig. 2(*a*). For the considered 1/8 unit cell, it is clear that the degrees of freedom of plane BEF in the *x* direction, plane AEH in the *y* direction, and plane ABCD in the *z* direction are fixed. However, the other three faces parallel to them can move in the corresponding directions. Furthermore, we can decompose the 1/8th representative volume element at each joint and obtain the force conditions of each beam [58], as illustrated in Fig. 2(*b*).

For each member of the 1/8th representative volume element, the effective loading and boundary conditions are identical, as shown in Fig. 2(*c*). We assume that forces $F_{1i} = F_{2i} = 1$ N and moments $M_i = 1\ N \cdot M$, for $i = m, n$, so that we can obtain the following parameters [57] by the force method of continuum mechanics:

$$\begin{cases} \delta_{F_{1i}F_{1i}} = \dfrac{a^3}{EI}\displaystyle\int_0^{\pi/2}\left(\frac{1}{i} - \frac{\sin\theta}{\sqrt{i^2\sin^2\theta + \cos^2\theta}}\right)^2 \frac{1}{\sqrt{i^2\sin^2\theta + \cos^2\theta}}d\theta \\ \delta_{F_{1i}F_{2i}} = -\dfrac{a^3}{EI}\displaystyle\int_0^{\pi/2}\left(\frac{1}{i} - \frac{\sin\theta}{\sqrt{i^2\sin^2\theta + \cos^2\theta}}\right)\frac{\cos\theta}{i^2\sin^2\theta + \cos^2\theta}d\theta \\ \delta_{F_{2i}F_{2i}} = \dfrac{a^3}{EI}\displaystyle\int_0^{\pi/2}\frac{\cos^2\theta}{\sqrt{i^2\sin^2\theta + \cos^2\theta}^3}d\theta \\ \delta_{M_iM_i} = \dfrac{a}{EI}\displaystyle\int_0^{\pi/2}\frac{1}{\sqrt{i^2\sin^2\theta + \cos^2\theta}}d\theta \\ \delta_{F_{2i}M_i} = \dfrac{a^2}{EI}\displaystyle\int_0^{\pi/2}\frac{\cos\theta}{i^2\sin^2\theta + \cos^2\theta}d\theta \\ \delta_{F_{1i}M_i} = -\dfrac{a^2}{EI}\displaystyle\int_0^{\pi/2}\left(\frac{1}{i} - \frac{\sin\theta}{\sqrt{i^2\sin^2\theta + \cos^2\theta}}\right)\frac{1}{\sqrt{i^2\sin^2\theta + \cos^2\theta}}d\theta \end{cases} \tag{1}$$

where $\delta_{jk} = \delta_{kj}$ is the displacement component in j direction introduced by the unit force in the k direction, and E and $I = bt^3/24$ represent Young's modulus of the raw material and the moment of inertia of the beam, respectively.

For beam AB, we can use the following equations to calculate the displacements in the F_{AB1}, F_{AB2}, and M_{AB} directions, respectively,

$$\begin{bmatrix} \delta_{F_{AB2}F_{AB1}} & \delta_{F_{AB2}F_{AB2}} & \delta_{F_{AB2}M_{AB}} \\ \delta_{F_{AB1}F_{AB1}} & \delta_{F_{AB1}F_{AB2}} & \delta_{F_{AB1}M_{AB}} \\ \delta_{M_{AB}F_{AB1}} & \delta_{M_{AB}F_{AB2}} & \delta_{M_{AB}M_{AB}} \end{bmatrix} \begin{bmatrix} F_{AB1} \\ F_{AB2} \\ M_{AB} \end{bmatrix} = \begin{bmatrix} u_A \\ v_B \\ 0 \end{bmatrix} \tag{2}$$

Similarly, for beam AD,

$$\begin{bmatrix} \delta_{F_{AD2}F_{AD1}} & \delta_{F_{AD2}F_{AD2}} & \delta_{F_{AD2}M_{AD}} \\ \delta_{F_{AD1}F_{AD1}} & \delta_{F_{AD1}F_{AD2}} & \delta_{F_{AD1}M_{AD}} \\ \delta_{M_{AD}F_{AD1}} & \delta_{M_{AD}F_{AD2}} & \delta_{M_{AD}M_{AD}} \end{bmatrix} \begin{bmatrix} F_{AD1} \\ F_{AD2} \\ M_{AD} \end{bmatrix} = \begin{bmatrix} u_D - u_A \\ v_D \\ 0 \end{bmatrix} \tag{3}$$

For beam BC,

$$\begin{bmatrix} \delta_{F_{BC2}F_{BC1}} & \delta_{F_{BC2}F_{BC2}} & \delta_{F_{BC2}M_{BC}} \\ \delta_{F_{BC1}F_{BC1}} & \delta_{F_{BC1}F_{BC2}} & \delta_{F_{BC1}M_{BC}} \\ \delta_{M_{BC}F_{BC1}} & \delta_{M_{BC}F_{BC2}} & \delta_{M_{BC}M_{BC}} \end{bmatrix} \begin{bmatrix} F_{BC1} \\ F_{BC2} \\ M_{BC} \end{bmatrix} = \begin{bmatrix} u_C \\ v_C - v_B \\ 0 \end{bmatrix} \tag{4}$$

For beam CD,

$$\begin{bmatrix} \delta_{F_{CD2}F_{CD1}} & \delta_{F_{CD2}F_{CD2}} & \delta_{F_{CD2}M_{CD}} \\ \delta_{F_{CD1}F_{CD1}} & \delta_{F_{CD1}F_{CD2}} & \delta_{F_{CD1}M_{CD}} \\ \delta_{M_{CD}F_{CD1}} & \delta_{M_{CD}F_{CD2}} & \delta_{M_{CD}M_{CD}} \end{bmatrix} \begin{bmatrix} F_{CD1} \\ F_{CD2} \\ M_{CD} \end{bmatrix} = \begin{bmatrix} u_D - u_C \\ v_C - v_D \\ 0 \end{bmatrix} \tag{5}$$

For beam AE,

$$\begin{bmatrix} \delta_{F_{AE2}F_{AE1}} & \delta_{F_{AE2}F_{AE2}} & \delta_{F_{AE2}M_{AE}} \\ \delta_{F_{AE1}F_{AE1}} & \delta_{F_{AE1}F_{AE2}} & \delta_{F_{AE1}M_{AE}} \\ \delta_{M_{AE}F_{AE1}} & \delta_{M_{AE}F_{AE2}} & \delta_{M_{AE}M_{AE}} \end{bmatrix} \begin{bmatrix} F_{AE1} \\ F_{AE2} \\ M_{AE} \end{bmatrix} = \begin{bmatrix} u_A \\ w_E \\ 0 \end{bmatrix} \tag{6}$$

For beam BF,

$$\begin{bmatrix} \delta_{F_{BF1}F_{BF1}} & \delta_{F_{BF1}F_{BF2}} & \delta_{F_{BF1}M_{BF}} \\ \delta_{F_{BF2}F_{BF1}} & \delta_{F_{BF2}F_{BF2}} & \delta_{F_{BF2}M_{BF}} \\ \delta_{M_{BF}F_{BF1}} & \delta_{M_{BF}F_{BF2}} & \delta_{M_{BF}M_{BF}} \end{bmatrix} \begin{bmatrix} F_{BF1} \\ F_{BF2} \\ M_{BF} \end{bmatrix} = \begin{bmatrix} v_F - v_B \\ w_F \\ 0 \end{bmatrix} \tag{7}$$

where

$$\begin{cases} \delta_{F_{AB2}F_{AB2}} = \delta_{F_{AD1}F_{AD1}} = \delta_{F_{BC1}F_{BC1}} = \delta_{F_{CD2}F_{CD2}} = \delta_{F_{1i}F_{1i}} \\ \delta_{F_{AB1}F_{AB1}} = \delta_{F_{AD2}F_{AD2}} = \delta_{F_{BC2}F_{BC2}} = \delta_{F_{CD1}F_{CD1}} = \delta_{F_{2i}F_{2i}} \\ \delta_{F_{AB1}F_{AB2}} = \delta_{F_{AD1}F_{AD2}} = \delta_{F_{BC1}F_{BC2}} = \delta_{F_{CD1}F_{CD2}} = \delta_{F_{1i}F_{2i}} \\ \delta_{F_{AB1}M_{AB}} = \delta_{F_{AD2}M_{AD}} = \delta_{F_{BC2}M_{BC}} = \delta_{F_{CD1}M_{CD}} = \delta_{F_{2i}M_i} \\ \delta_{F_{AB2}M_{AB}} = \delta_{F_{AD1}M_{AD}} = \delta_{F_{BC1}M_{BC}} = \delta_{F_{CD2}M_{CD}} = \delta_{F_{1i}M_i} \\ \delta_{M_{AB}M_{AB}} = \delta_{M_{AD}M_{AD}} = \delta_{M_{BC}M_{BC}} = \delta_{M_{CD}M_{CD}} = \delta_{M_iM_i} \end{cases} \tag{8}$$

for $i = m$ and

$$\begin{cases} \delta_{F_{AE2}F_{AE2}} = \delta_{F_{BF1}F_{BF1}} = \delta_{F_{1i}F_{1i}} \\ \delta_{F_{AE1}F_{AE1}} = \delta_{F_{BF2}F_{BF2}} = \delta_{F_{2i}F_{2i}} \\ \delta_{F_{AE2}F_{AE1}} = \delta_{F_{BF1}F_{BF2}} = \delta_{F_{1i}F_{2i}} \\ \delta_{F_{AE1}M_{AE}} = \delta_{F_{BF2}M_{BF}} = \delta_{F_{2i}M_i} \\ \delta_{F_{AE2}M_{AE}} = \delta_{F_{BF1}M_{BF}} = \delta_{F_{1i}M_i} \\ \delta_{M_{AE}M_{AE}} = \delta_{M_{BF}M_{BF}} = \delta_{M_iM_i} \end{cases} \tag{9}$$

for $i = n$.

The physical meaning of the third row of each matrix is that the rotational angle at each endpoint is 0.

Based on the periodicity and the symmetry of the structure, the displacement-matching conditions at each endpoint can be acquired [48]:

$$\begin{cases} u_D = u_G = u_H \\ v_C = v_F = v_G \\ w_E = w_F = w_G = w_H \\ u_A = u_G - u_C \\ v_B = v_G - v_D \end{cases} \tag{10}$$

During the quasi-static loading, the force equilibrium conditions are always suitable for each endpoint. Based on the force balance at point A in the x direction, we have

$$F_{AB2} + F_{AE2} - F_{AD2} = 0 \tag{11}$$

and the force equilibrium is also satisfied at point B in the y direction,

$$F_{AB1} - F_{BC1} - F_{BF1} = 0 \tag{12}$$

Due to all degrees of freedom of plane CFG in the y direction being free, the total force along the y direction in this surface should be 0, that is,

$$F_{BF1} + F_{BC1} + F_{CD1} = 0 \tag{13}$$

Similarly, we have the same force conditions for plane DGH in the x direction:

$$F_{AE2} + F_{AD2} + F_{CD2} = 0 \tag{14}$$

Moreover, the relationship between effective stress and effective strain in the z direction is

$$2(F_{AE1} + F_{BF2}) = \sigma_z \left(a + \frac{a}{m} + t\right)^2 \tag{15}$$

So, the effective strain of the structure in the x and the z directions can be calculated as

$$\begin{cases} \varepsilon_x = \dfrac{u_D}{a + (a/m) + t} \\ \varepsilon_z = \dfrac{w_E}{(a/n) + (t/2)} \end{cases} \tag{16}$$

Finally, the effective elastic constants, i.e., the effective Poisson's ratio and normalized Young's modulus, of the proposed metamaterial can be obtained:

$$\begin{cases} \nu_{zx} = -\dfrac{\varepsilon_x}{\varepsilon_z} \\ \hat{E}_{zn} = \dfrac{\sigma_z}{E\varepsilon_z} \end{cases} \tag{17}$$

3.4 Simulations. Numerical calculations were performed using the commercial software COMSOL MULTIPHYSICS 6.0 with the Structural Mechanics module. First of all, the computer-aided design (CAD) model of the unit cell (see Fig. 1(*c*)) was built in software CATIA V5R20, and then the model was imported into COMSOL MULTIPHYSICS 6.0. It was assumed that the material that the unit cell is made of has the same properties as the bulk material used during the fabrication process. Thus, the isotropic material assigned to the model was characterized by Young's modulus of 4 GPa, Poisson's ratio equal to 0.3, and density set to be 1190 kg/m^3. To explore the structural nonlinearity of the unit cell under large deformations, elastoplasticity of the raw material was ignored in this simulation. In addition, periodic boundary conditions were applied to all three principal directions. It is worth noting that all boundary surfaces of the unit cell remain planar after deformation since only a metamaterial under longitudinal compression is taken into account in this work. The same boundary conditions are applied to the theoretical model, as discussed in the previous subsection. For the static compression simulations, the periodicity is set as

$$\begin{bmatrix} u_{dst} \\ v_{dst} \\ w_{dst} \end{bmatrix} = \begin{bmatrix} i & j & k \end{bmatrix} \begin{bmatrix} u_{src} \\ v_{src} \\ w_{src} \end{bmatrix} \tag{18}$$

where "dst" is the destination and "src" is the source. If the plane is perpendicular to the x direction, $i = -1$, and $j = k = 1$. If the plane is perpendicular to the y or z directions, similar rules apply, i.e., $j = -1$, $i = k = 1$ and $k = -1$, $i = j = 1$, respectively. For the computation of

dispersion relations, Floquet–Bloch periodicity was applied to the primitive unit cell. The first Brillouin zone of the unit cell is shown as an insert in Fig. 5(*a*) [59]. For elliptical rings in the *xz* and *yz* planes, the "contact pair" is defined between their outer surface and their neighbor in the *z* direction. The augmented Lagrangian method and equations were used to describe the contact properties. The entire structure is meshed by approximately 30,000 free tetrahedral elements. Finally, the prestressed eigenfrequency module is used to obtain the dispersion relation. More specifically, the computation process is divided into two steps. In the first step, the stationary module is employed to apply a prescribed displacement to the metamaterial in the *z* direction. For instance, in the case of the unit cell with a 20 μm prescribed displacement, displacements of -10 μm and 10 μm are imposed to the top and bottom boundary surfaces of the unit cell along the *z* direction. In the second step, the eigenfrequency module is used to calculate the dispersion relation. It is worth noting that the computation in the second step depends on the results from the first step, since stresses are introduced in each curved beam. Hence, the prescribed deformations and the dispersion relations of the considered metamaterial must be computed step by step.

4 Results and Discussion

4.1 Effective Mechanical Properties of the Proposed Meta materials. To explore the influence of the shape of each elliptical ring, described by parameters *m* and *n*, on effective elastic constants, a theoretical model was built based on the theory of beams [57,58] (see Sec. 3). Effective elastic constants of the metamaterial under small deformations obtained by different methods are compared in Fig. 3(*a*). As a note, the effective elastic constants under small deformation in experimental and numerical results are calculated from the slope of the curves for compressive strain ranging from 0 to 0.05. This method is different from the method used in the following subsection to compute the elastic constants at different steps since in the latter case the metamaterial is significantly deformed. The results shown in Fig. 3(*a*) validate the theoretical model built in this work, as the results obtained by these three methods match well. The variations predicted by the theoretical model of the effective Poisson's ratio and the normalized effective modulus of the metamaterial with *m* and *n* varying in the range from 0.7 to 3 are shown in Figs. 3(*b*) and 3(*c*). In general, both *m* and *n* significantly impact the effective constants.

The following points are highlighted. First, only the shape of the elliptical ring in the *xy* plane, controlled by parameter *m*, determines the auxeticity of the entire structure, i.e., the sign of the effective Poisson's ratio. As demonstrated by Fig. 3(*b*), if *m* is smaller than 1.1, the metamaterial is nonauxetic, and if $m > 1.1$, it is auxetic. Hence, the shape of the elliptical ring in the *xz* plane, controlled by the parameter *n*, does not influence the sign of the effective Poisson's ratio. This deformation property is the reason for the metamaterial undergoes an elastically stable continuous phase transition of the Poisson's ratio, as we reported in another work [48]. Second, when parameters *m* and *n* are in the range [0.7, 3], their influences on the normalized effective modulus are opposite. An increasing value for *m* and *n* means a decrease in the aspect ratio of the curved beam in each elliptical ring. In other words, the curved beam tends toward a straight beam with increasing *m* and *n*. The curved beam in the *xy* plane with a smaller aspect ratio (larger *m*) enhances the constraint of deformation of the whole structure and increases the modulus of the system. Conversely, the smaller aspect ratio of the curved beam in the *xz* plane (larger *n*) has a negative influence on the force transmission in the *z* direction and thus decreases the modulus of the system. These are fundamental reasons why parameters *m* and *n* have opposite effects on the normalized effective modulus.

More importantly, the theoretical predictions imply that both auxeticity and effective Young's modulus of the metamaterial will be enhanced with the lessening of parameter *n*, if the value of parameter *m* is close to 2, as demonstrated in dotted lines and arrows in Fig. 3. In other words, it is possible to magnify the aspect ratio (corresponding to the reducing of parameter *n*) of the elliptical rings in the *xz* and *yz* planes to cement the elastic properties of the metamaterial when the shape of elliptical rings in the *xy* plane remains constant. This point can provide fundamental insights into the multistep behavior of the metamaterial which will be discussed in detail in the following subsections.

4.2 Multistep Behavior and Tunable Elastic Constants. This subsection focuses on the experimental and numerical investigation of the multistep behavior and tunable mechanical properties of the designed metamaterial under large compressive deformation. The samples studied in this subsection are fabricated by the two-photon lithography 3D printing (see Sec. 3) technology with IP-S resin (with Young's modulus 4 GPa, Poisson's ratio 0.3 and density 1190 kg/m^3), as illustrated in Figs. 1(*d*)–1(*f*). The geometrical parameters of the samples have been set as $m = n = 1.97$, $a = 75$ μm, $t = 10$ μm, $b = 16$ μm, and $t_c = 0.5$ μm, respectively.

Experimental and numerical results are presented in Fig. 4. In both experimental and numerical results, the reaction force divided by the cross section of the samples and the deformation

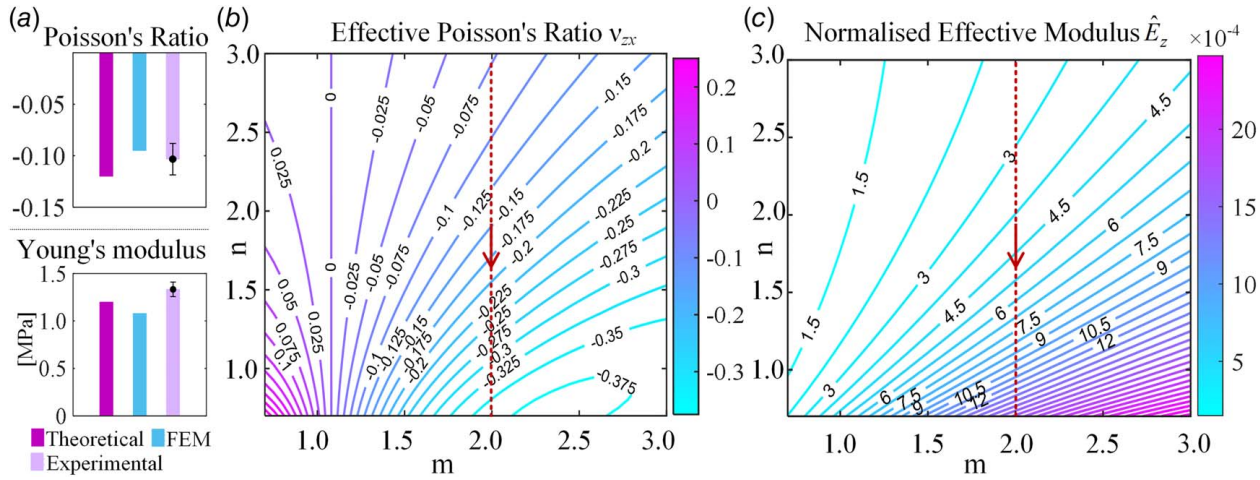

Fig. 3 Effective Young's modulus and auxeticity of the proposed metamaterials: (*a*) Effective elastic constants of the metamaterial under small deformations obtained by different methods are compared, (*b*) the trend in the effective Poisson's ratio is shown as a function of the change in *m* and *n*, and (c) the variation of the normalized effective modulus versus the geometric parameters. Other parameters set as $a = 75$ μm, $t = 10$ μm, $b = 16$ μm, and $t_c = 0.5$ μm.

between top and bottom boundary surfaces divided by the size of the samples in the z direction were used respectively to compute the effective stress (σ_z) and effective strain (ε_z). The lateral deformation in the central region of the sample is divided by the original size of this region to calculate the effective lateral strain (ε_x). The experimental effective elastic constants, i.e., lateral strain ε_x and compression stress σ_z versus compressive strain ε_z, are shown in Figs. 4(*a*)–4(*d*). Herein, we resolve the whole compression process into two main steps, called step 1 and step 2. As can be seen in Fig. 4, the lateral strain ε_x and the compressive stress σ_z exhibit completely different trends in either step. To ascribe effective elastic constants to the metamaterial at each step, the slope of the lateral strain versus vertical strain and the counterpart of the compressive stress versus compressive strain at each step were used to figure out the corresponding effective Poisson's ratio and Young's modulus. With this definition, the effective elastic constants for each step are reported in Figs. 4(*b*) and 4(*d*). It is clear that both the effective Poisson's ratio ν_{zx} and Young's modulus E_z of the metamaterial are enhanced when the compression process jumps from step 1 to step 2. $\nu_{zx} = -0.12$ and $E_z = 1.2$ MPa for the first step and $\nu_{zx} = -0.3$ and $E_z = 2.6$ MPa for the second step. Significantly, the numerical results obtained with finite element method (FEM) confirm the variations of the elastic constants, as Fig. 4(*h*) shows.

To reveal the nature of variations of the elastic constants in either step, experimental and numerical compressive deformations are reported in Figs. 4(*e*)–4(*f*), respectively. It is worth noting that the outer surface of the curved beams which are in the xz and yz planes contact the counterparts of their neighbors in the z direction if the compression strain reaches a critical value, equal to 30% in experiments and to 26% in simulations. This self-contact is the key element that enhances the elastic constants and marks the separation between steps due to the resulting modification of the effective geometrical parameter of the unit cell. As a matter of fact, after contact the effective aspect ratios of the curved beams in the xz and yz planes increase, as highlighted by the green curves in Fig. 4(*f*). This increase in the aspect ratio of curved beams enhances the force transmission in the z direction. The aspect ratio of the curved beam in the xy plane, however, remains unchanged at the critical strain (the strain at the onset of contact) for step 1 and step 2. Hence, the contact alters the shape of the curved beams in the vertical direction but does not modify the configuration of the curved beam in the horizontal direction, as demonstrated in Fig. 4(*f*). More specifically, the effective value of n decreases, whereas m remains unchanged, so that the geometric parameters of the unit cell jump directly from one point to another along the arrow direction with the red dotted line in Figs. 3(*b*) and 3(*c*). As a result, both auxeticity and Young's modulus

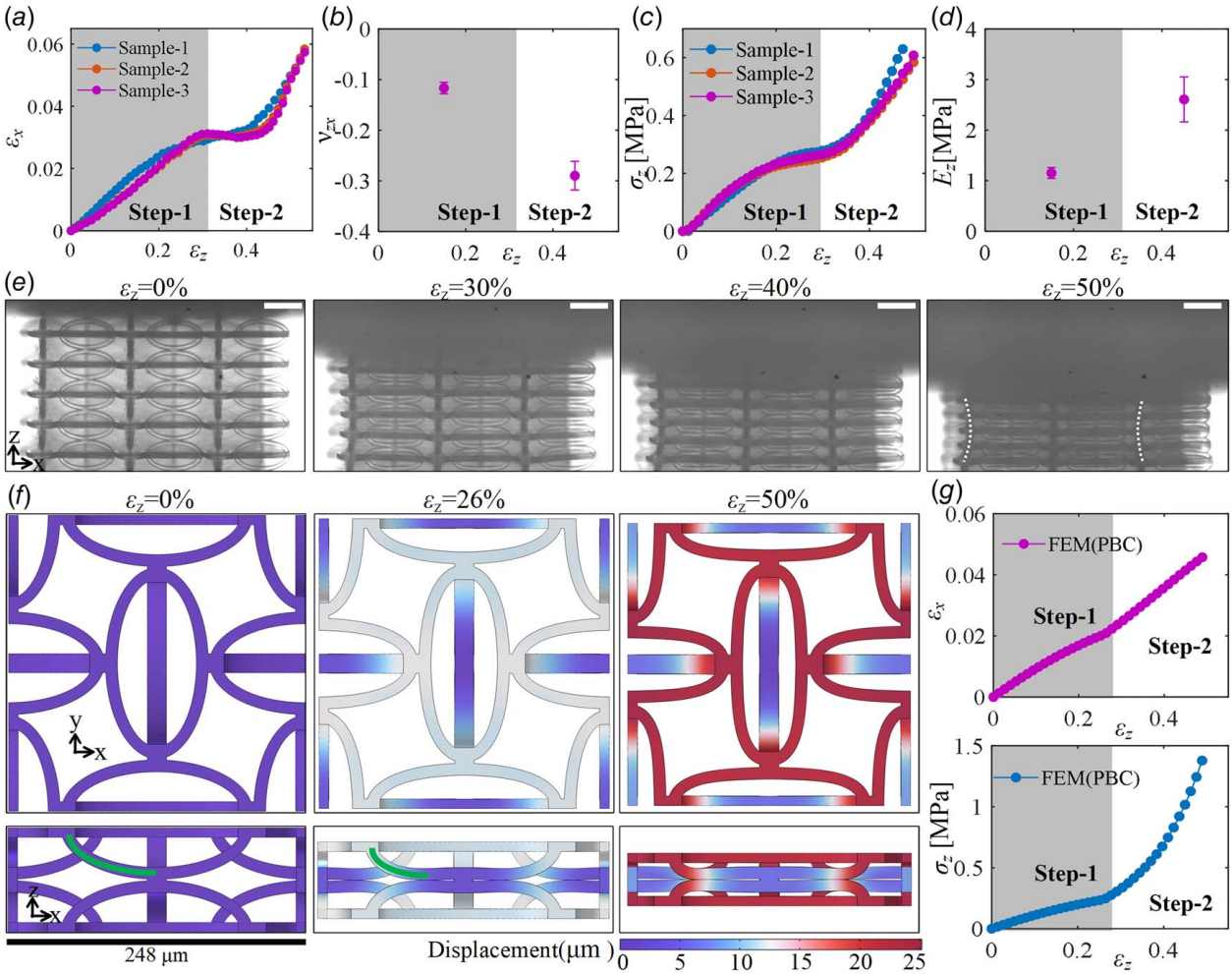

Fig. 4 Multistep behavior and tunable elastic constants during the compression along the z direction: (*a*) normalized strain ε_x versus normalized strain ε_z, (*b*) effective Poisson's ratio for step 1 and step 2, (*c*) normalized stress σ_z versus normalized strain ε_z, (*d*) effective Young's modulus for both steps, (e) experimental compression deformation (the scale bar length is 100 μm), (*f*) Numerical compressive deformation process of the conventional unit cell under periodic boundary conditions (PBC) applied in all three main directions. The contour plot shows the magnitude of the displacement, and (*g*) normalized strain ε_x and normalized stress σ_z versus ε_z obtained by the FEM.

are enhanced, in good agreement with the prediction of the theoretical model in Figs. 3(*b*) and 3(*c*), as discussed in the last paragraph in the previous subsection. It is worth noting that the theoretical prediction of the elastic constants assumes small deformations. They can hardly, in principle, quantify the variation of the elastic constants of the metamaterial after contact. Nevertheless, they still provide a qualitative trend. Another essential point is that the whole system remains elastically stable during the entire compression process, i.e., during both step 1 and step 2, without any instability of the structure or postbuckling of the raw material [48].

There are some differences between experimental and numerical results. For instance, in both experimental $\varepsilon_x(\varepsilon_z)$ and $\sigma_z(\varepsilon_z)$ curves, short plateaus can be observed. In contrast, they do not appear in the simulation results, since the elastoplasticity of the raw material is ignored in the computational model. Simulation results merely show the geometric nonlinearity of the structure, but experimental results further include the geometric and material nonlinearity of the structure and the raw material. This is one of the reasons why Young's modulus for step 2 in experiments is smaller than in simulation. Additionally, the experimental samples are composed of a limited number of unit cells, so boundary effects cannot be absolutely eliminated. More importantly, friction between the top and bottom surfaces of the samples and the mechanical testing machine limits the lateral contraction of these surfaces. In this case, the samples are deformed like a reentrant structure during the compression process, that is the area of the cross section of the central surface is smaller than the counterparts of the top and bottom surfaces, as shown with the white dashed line in Fig. 4(*e*). This reentrant deformation further enhances the auxeticity of the metamaterial in the experimental tests. Conversely, the simulation model assumes periodic boundary conditions in all three principal directions so that no reentrant deformation of the unit cell can be observed during the entire compression process, as shown in Fig. 4(*f*). This is the main reason why the experimental auxeticity for step 2 surpasses the numerical auxeticity. Anyway, the predictions of the theoretical model and the experimental and simulation results all imply the same trends for the multistep mechanical behaviors of the considered metamaterials.

4.3 Potential Application to Tunable Phononic Band Gap Structures. As discussed in the previous subsections, the proposed metamaterial shows different elastic constants depending on the compression strain, as if there were two different materials. Here, we want to highlight a potential application to tunable phononic band gap structures. It may not be immediately apparent, but a varying Poisson's ratio causes a modulation of the volume and hence of the relative density of porous structures and materials since the overall mass is conserved. This effect is especially strong under large compressive or stretching strain. Furthermore, Young's modulus also varies a lot with the applied strain, as we discussed above. As a result, both the relative density and the modulus, but also all effective elastic constants of the metamaterial vary with the applied strain. As a matter of fact, the dispersion of acoustic and elastic waves is highly dependent on the density and the modulus of materials [60–62].

Herein, based on the principle of local resonance [41], physically concentrated masses are added at the nodes connecting elliptical rings in the z direction, as shown in Fig. 5(*a*). The essential property of the physically concentrated masses is that they change the dynamic mechanical properties of the metamaterial without changing its static mechanical properties. This type of mass can be fabricated with the same raw material as the structure, implying that limited challenges are added to the manufacturing process. If a predisplacement of 30 μm is applied in the z direction, the structure deforms from step 1 (in Fig. 5(*b*)) to step 2 (in Fig. 5(*c*)). At the transition between the steps, the outer surfaces of the curved beams in the z direction contact with their neighbors as discussed previously.

The phononic band structure for elastic waves propagating along the z direction is shown in Fig. 5(*d*). As apparent in Fig. 5(*d*), α, the first band gap of the structure appears in the range between 255 kHz and 285 kHz. It does not shift significantly with the predisplacement within step 1, as exemplified by panels Fig. 5(*d*), β and γ. The first band gap however shifts to the range between 885 kHz and 955 kHz when a predisplacement of 30 μm is applied to the structure along the z direction, i.e., by more than a factor three, as shown in Fig. 5(*e*). To prove that the band gap shift from Figs. 5(*d*)–5(*e*) is introduced by the multistep behavior of the metamaterial rather than by the prestress of each curved beam, the evolution of the phononic band structure under different predisplacements is compared in Fig. 5(*d*). Obviously, within step 1, the frequency range of the first band gap does not change significantly with the predisplacement. The observed changes are attributed mainly to the prestress of each curved beam. In step 2, however, the variation of the first band gap is introduced by the contact between curved beams. As a note, it exceeds the mere change of effective velocity at low frequency implied by the static measurement of Young's modulus reported in Fig. 4.

The results demonstrated in this subsection suggest potential applications of the studied metamaterials in dynamics. First, elastic wave dispersion relies on both the added physical concentrated masses and the mechanical properties of the original structure (the structure studied in the last subsection), implying a high degree of design flexibility. Second, after fabrication variable dispersion properties are obtained only via external compression excitation. This feature decreases the requirements on the operating environment needed to obtain adjustable dispersion behaviors. Finally, during the compression process, the metamaterial does not occupy any additional space thanks to its auxeticity. Hence, this type of metamaterial could be used in micro/nanosystems or space-limited devices.

4.4 Delocalization of Deformations and Reusability of the Metamaterial. Structures and materials hardly keep constant mechanical properties and thus remain reusable after undergoing cycles of large deformations. This is usually due to two essential elements, elastoplasticity and the failure mode of the materials. Localized deformations of structures and materials lead to downright failure. Examples are the collapse of lightweight porous structures (or the postbulking or the instability of their elements), the shear banding in metallic materials, and the propagation of cracks in ceramics. The aforementioned localized deformations limit applications to small strain scenarios. From the mechanical point of view, the occurrence of the initial peak or of the first negative stiffness event in a strain–stress curve implies unstable deformation. Specifically, for periodically porous structures, the localized deformation of the random layer is an indication of a systemic level instability or failure [63].

To obtain reusable 3D mechanical metamaterials, we fabricated the designed metamaterial with TPU using the selective laser sintering 3D printing technology at the centimeter scale, as shown in Fig. 6(*a*). For TPU, Young's modulus is 27 MPa, Poisson's ratio is 0.45, density is 1200 kg/m^3, and the elongation of the raw material is 500%. A cycle of five compressive tests with 60% compression strain was employed to evaluate the reusable mechanical response of the metamaterial. After the compressive tests, the loss of the metamaterial is limited, as Fig. 6(*b*) shows. The responses and deformations are reported in Figs. 6(*c*)–6(*h*). To describe the effective properties precisely, the slope of the curves is averaged between 0–40% and 40–60% compression strain to compute the effective properties for each step, as reported in Figs. 6(*d*) and 6(*f*). Although the curves show slight nonlinearity, the initial peak or the first negative stiffness event is never observed. The effective Poisson's ratio changes from −0.08 to −0.13 between step 1 and step 2, whereas Young's modulus concurrently changes from 0.20 MPa to 1.62 MPa.

The metamaterial exhibits stable auxeticity and positive stiffness under large compression deformation, i.e., the corresponding compression strain reaches 60%. These results can be explained based

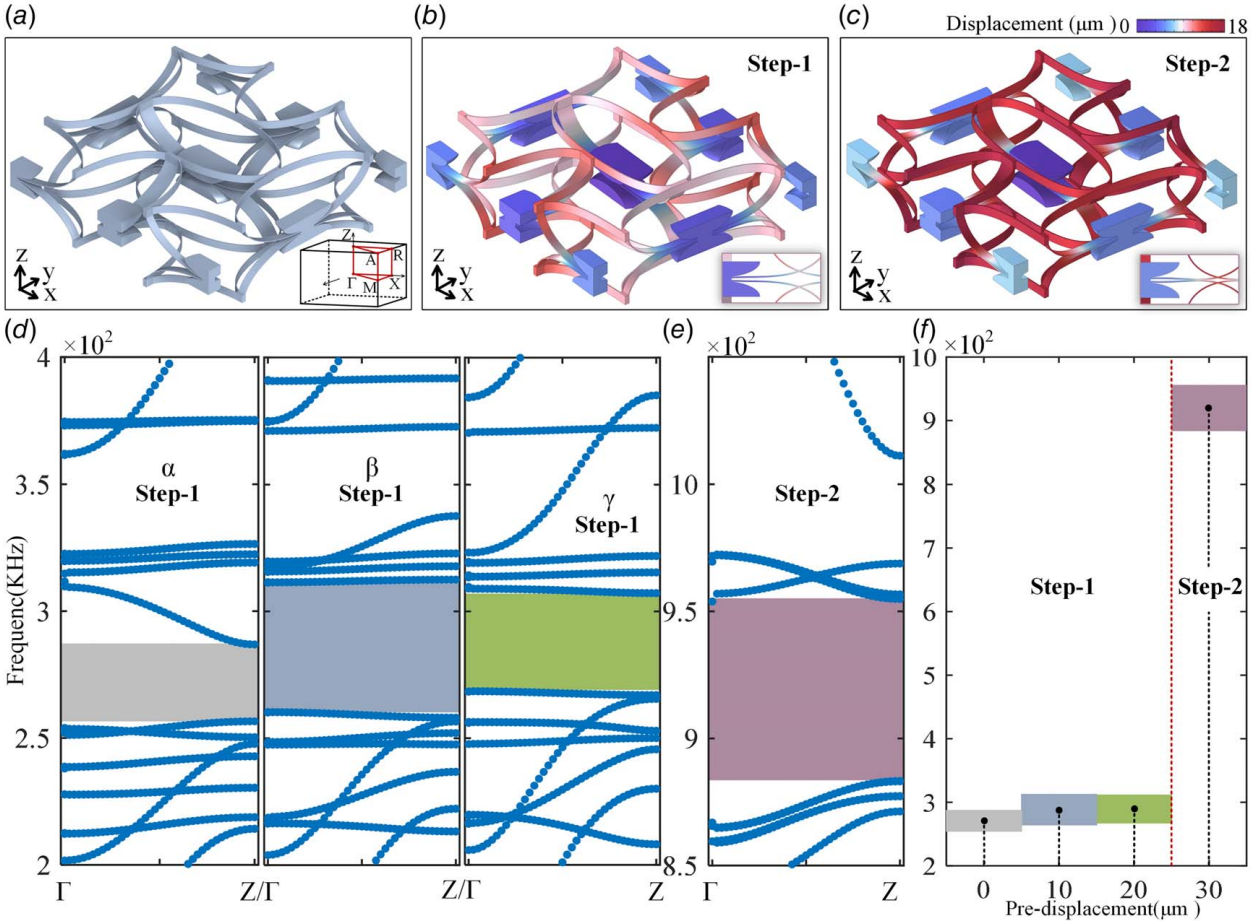

Fig. 5 Potential application to the design of structures with a tunable phononic band gap: (*a*) a physical concentrated mass is added at the connecting node of the curved beams. The geometry parameters are set as $a = 79.5\ \mu$m, $t = 1\ \mu$m, $b = 16\ \mu$m, $t_c = 0.5\ \mu$m, and $m = n = 1.87$, (*b*) the structure undergoes a predisplacement of 20 μm in step 1, (c) the structure undergoes a predisplacement of 30 μm in step 2, (*d*) the phononic band structure for elastic waves propagating in the *z* direction is shown for step 1 (α, β, and γ correspond to the structure subjected to a predisplacement of 0 μm, 10 μm, and 20 μm, respectively), (e) the phononic band structure for elastic waves propagating in the *z* direction is shown for a predisplacement 30 μm, i.e., for step 2, and (*f*) the frequency range of the first band gap is plotted as a function of the predisplacement.

on the delocalization of deformations inside the metamaterial that occurs thanks to its multistep behavior. Different mechanism-based multistep behaviors can lead to localized [64] or delocalized [63] response of metamaterials. As a matter of fact, the multistep behavior presented in this work averts the occurrence of localized deformations of the metamaterial thanks to the self-contact of the outer surfaces of the elliptical rings eliminating instabilities of curved beams, which is a property that matte geometries lack [48]. Significantly, the variations of the effective Poisson's ratio and modulus with TPU show less nonlinearity than their counterparts with the photopolymer of the previous subsection. This highlights the importance of the choice of raw material. Another important point is that the critical strain separating step 1 and step 2 depends on the length of the connector between each curved beam in the z direction, i.e., on the parameter t_c. If the value of parameter t_c is large enough, the outer surface of the elliptical rings along the z direction will never contact their neighbors during the entire compression process. Under this circumstance, the multistep behavior will be eliminated. On the contrary, contact can be accelerated by diminishing parameter t_c, which means reducing the critical strain between step 1 and step 2. Adjustment of this parameter leads to the design flexibility of the multistep behaviors.

Reusability of auxetic metamaterials is very important, particularly when they work as functional materials. It here highly relies on the hyperelastic behavior of the raw material TPU. As Figs. 6(*c*) and 6(*d*) show, the auxeticity of the metamaterial remains identical during the five cycles. In contrast, Young's modulus in step 1 of the first cycle is slightly larger than for the subsequent cycles, as shown in Figs. 6(*e*) and 6(*f*). We think that some initial stress, generated during the fabricating process, is eliminated by the first compression cycle so that the next four cycles show a nearly identical effective Young's modulus. The analogous scenario is not observed for auxeticity since the effective Poisson's ratio of the metamaterial is independent of the properties of the raw material. Figures 6(*g*) and 6(*h*) demonstrate the deformation of metamaterials from different viewing angles and under a different number of cycles. Figure 6(*g*) shows the deformation in the front view during the first cycle while Fig. 6(*h*) shows the deformation of the side view during the fifth cycle. The nephogram in Fig. 6(*g*) indicates the displacement along the x direction. The morphing of the left region and the right region of the sample imply the lateral contraction deformation during compression loading, that is, auxeticity of the considered metamaterial. The reusability of the metamaterial under large compression makes it potentially attractive for applications in some functional fields. For example, the proposed metamaterial can be used many times in engineering fields with time-varying requirements for load-bearing capacity but also lateral and longitudinal space.

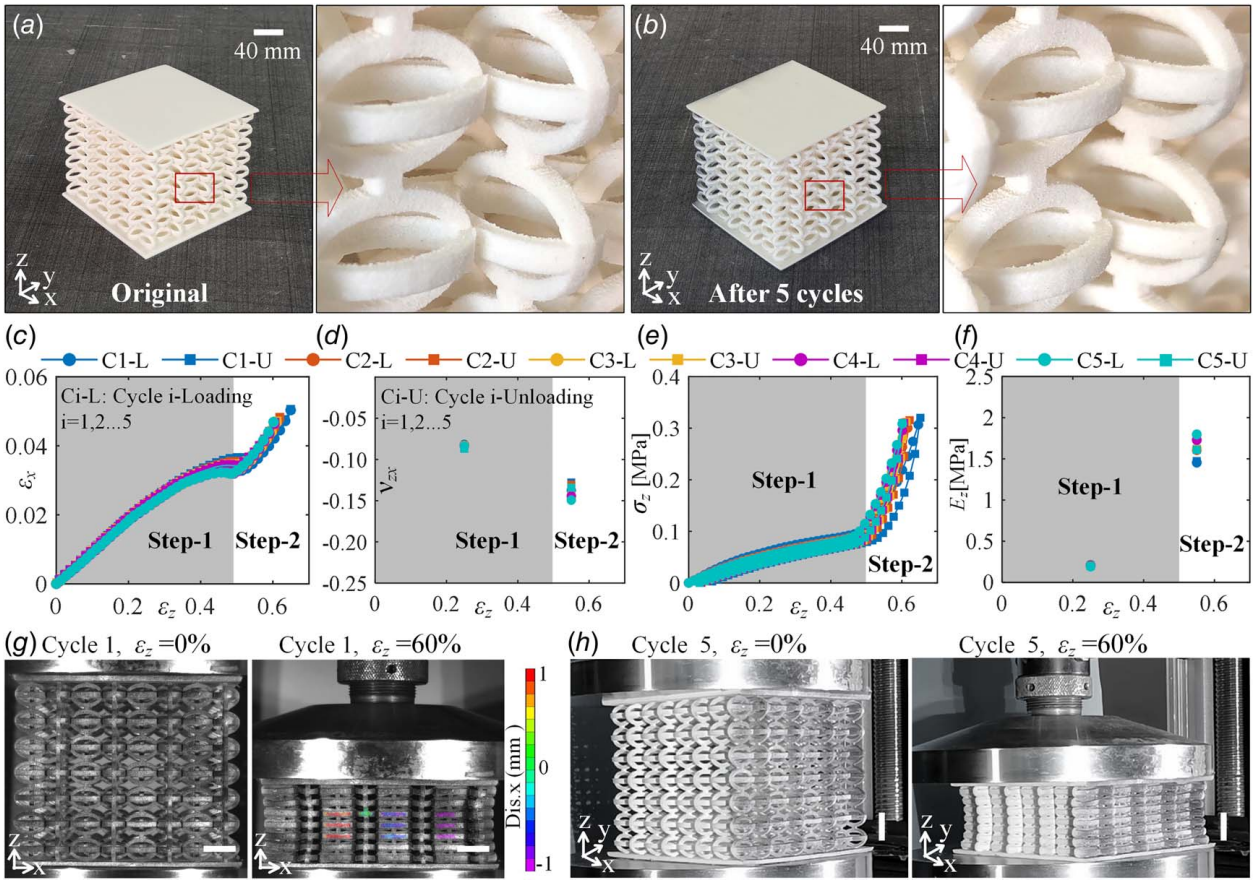

Fig. 6 Delocalization of deformations and reusability under large compressive strain. (*a*) The original metamaterial composed of $4 \times 4 \times 7$ unit cells was fabricated by TPU. The geometry parameters are set as $a = 9$ mm, $t = 2$ mm, $b = 3$ mm, $t_c = 1$ mm, and $m = n = 1.59$. (*b*) The metamaterial after five compression tests. (c) Normalized strain ε_x versus normalized strain ε_z. (*d*) Effective Poisson's ratio. (e) Normalized stress σ_z versus normalized strain ε_z. (*f*) Effective Young's modulus. $C_i - L(U)$, $M = 1, 2, \ldots, 5$, represents the loading (L) or unloading (U) curves of the ith cycle. Deformation of the metamaterial under different compressive strains and cycles ((*g*) for the first cycle and (*h*) for the fifth cycle). The length of the scale bar is 20 mm. The pictures in panel (*g*) are output from a commercial DIC software and the nephogram indicates the displacement along the x direction.

5 Conclusions

In conclusion, we have introduced a 3D mechanical metamaterial with multistep mechanical properties under variable applied strain in this article. The metamaterial has a weaker auxeticity and modulus in step 1 but stronger counterparts in step 2. This concept has been demonstrated using a single constituent material structure. Both the instabilities of the elements and the postbuckling of the materials are prevented, which means the whole system remains elastically stable states during the compression process. In addition, the transformation between the two steps solely depends on the applied compressive strain. The multistep behaviors of the proposed metamaterial could be used to design periodic structures with tunable phononic band gaps. Finally, the contact-based multistep behavior avoids the occurrence of instabilities in the curved beams during the delocalization deformation of the metamaterial that occurs under large compression strains. Reusability of the metamaterial is enabled by the hyperelastic raw material TPU. This study may spur the development of metamaterial with tunable static mechanical properties and multifunctional applications. In the future, the following two aspects may be taken into account when designing metamaterials with tunable mechanical properties. On the one hand, designing metamaterials with identical expected tunable behavior in all three principal directions could address the anisotropy of the current work. On the other hand, constructing metamaterials with special adjustable mechanical properties both under compression and tension mechanical environment is attractive and valuable.

Acknowledgment

This work was supported by the National Key Research and Development Program of China, the EIPHI Graduate School of UBFC, the French Investissements d'Avenir program, in part by the ANR PNanoBot and ANR OPTOBOTS project, the French RENATECH network and its FEMTO-ST technological facility, the National Natural Science Foundation of China, and the China Scholarship Council. L. Wang and X. Niu acknowledge the support of the Hong Kong Research Grants Council (HKRGC) General Research Fund (GRF). K.K. Dudek acknowledges the support of the Polish National Science Centre (NCN) in the form of the grant awarded as a part of the SONATA 18 program.

Funding Data

- The National Key Research and Development Program of China (National Key R&D Program of China, grant number 2022YFB3707800).
- Agence Nationale de la Recherche (ANR, grant numbers ANR-17-EURE-0002, ANR-21-CE33-0015, ANR-21-CE33-0003).

- The National Natural Science Foundation of China (NSFC, grant number 11972008).
- The China Scholarship Council (CSC, grant number 202106120088).
- The Hong Kong Research Grants Council (HKRGC) General Research Fund (GRF, grant number 11302920).
- The Polish National Science Centre (NCN, grant number No. 2022/47/D/ST5/00280).

Conflict of Interest

There are no conflicts of interest.

Data Availability Statement

The authors attest that all data for this study are included in the article.

References

[1] Frenzel, T., Kadic, M., and Wegener, M., 2017, "Three-Dimensional Mechanical Metamaterials With a Twist," Science, **358**(6366), pp. 1072–1074.

[2] Soukoulis, C. M., Linden, S., and Wegener, M., 2007, "Negative Refractive Index at Optical Wavelengths," Science, **315**(5808), pp. 47–49.

[3] Milton, G., 2002, *The Theory of Composites (Cambridge Monographs on Applied and Computational Mathematics)*, Cambridge University Press, Cambridge, UK.

[4] Kadic, M., Milton, G. W., van Hecke, M., and Wegener, M., 2019, "3D Metamaterials," Nat. Rev. Phys., **1**(3), pp. 198–210.

[5] Chen, Y., Abouelatta, M. A., Wang, K., Kadic, M., and Wegener, M., 2023, "Nonlocal Cable-Network Metamaterials," Adv. Mater, **35**(15), p. 2209988.

[6] Craster, R., Guenneau, S., Muamer, K., and Wegener, M., 2023, "Mechanical Metamaterials," Rep. Prog. Phys. Phys. Soc. (Great Britain), **86**(9), p. 094501.

[7] Coulais, C., Sounas, D., and Alu, A., 2017, "Static Non-Reciprocity in Mechanical Metamaterials," Nature, **542**(7642), pp. 461–464.

[8] Coulais, C., Sabbadini, A., Vink, F., and van Hecke, M., 2018, "Multi-Step Self-Guided Pathways for Shape-Changing Metamaterials," Nature, **561**(7724), pp. 512–515.

[9] Grima, J. N., and Evans, K. E., 2000, "Auxetic Behavior From Rotating Squares," J. Mater. Sci. Lett., **19**(17), pp. 1563–1565.

[10] Grima, J. N., Jackson, R., Alderson, A., and Evans, K. E., 2000, "Do Zeolites Have Negative Poisson's Ratios?" Adv. Mater., **12**(24), pp. 1912–1918.

[11] Grima, J. N., Winczewski, S., Mizzi, L., Grech, M. C., Cauchi, R., Gatt, R., Attard, D., Wojciechowski, K. W., and Rybicki, J., 2015, "Tailoring Graphene to Achieve Negative Poisson's Ratio Properties," Adv. Mater., **27**(8), pp. 1455–1459.

[12] Ghatak, A., Brandenbourger, M., Van Wezel, J., and Coulais, C., 2020, "Observation of Non-Hermitian Topology and Its Bulk–Edge Correspondence in an Active Mechanical Metamaterial," Proc. Natl. Acad. Sci. U.S.A., **117**(47), pp. 29561–29568.

[13] Coulais, C., Teomy, E., De Reus, K., Shokef, Y., and Van Hecke, M., 2016, "Combinatorial Design of Textured Mechanical Metamaterials," Nature, **535**(7613), pp. 529–532.

[14] Qu, J., Gerber, A., Mayer, F., Kadic, M., and Wegener, M., 2017, "Experiments on Metamaterials With Negative Effective Static Compressibility," Phys. Rev. X, **7**(4), p. 041060.

[15] Zhang, H., Zhang, W., Liao, Y., Zhou, X., Li, J., Hu, G., and Zhang, X., 2020, "Creation of Acoustic Vortex Knots," Nat. Commun., **11**(1), p. 3956.

[16] Chen, Y., Li, X., Hu, G., Haberman, M. R., and Huang, G., 2020, "An Active Mechanical Willis Meta-Layer With Asymmetric Polarizabilities," Nat. Commun., **11**(3681), pp. 1–8.

[17] Wang, Z., Zhang, Q., Zhang, K., and Hu, G., 2016, "Tunable Digital Metamaterial for Broadband Vibration Isolation at Low Frequency," Adv. Mater., **28**(44), pp. 9857–9861.

[18] Antonakakis, T., Craster, R. V., and Guenneau, S., 2013, "Asymptotics for Metamaterials and Photonic Crystals," Proc. R. Soc. A, **469**(2152), p. 20120533.

[19] Guenneau, S., and Craster, R. V., 2013, "Fundamentals of Acoustic Metamaterials," *Acoustic Metamaterials: Negative Refraction Imaging, Lensing Cloaking*, R. V. Craster, and S. Guenneau, eds., 1st ed., Springer, London, UK, pp. 1–42.

[20] Wu, Q., Zhang, X., Shivashankar, P., Chen, Y., and Huang, G., 2022, "Independent Flexural Wave Frequency Conversion by a Linear Active Metalayer," Phys. Rev. Lett., **128**(24), p. 244301.

[21] Chen, Y., Li, X., Scheibner, C., Vitelli, V., and Huang, G., 2021, "Realization of Active Metamaterials With Odd Micropolar Elasticity," Nat. Commun., **12**(1), p. 5935.

[22] Chen, X., Moughames, J., Ji, Q., Martínez, J. A., Tan, H., Ulliac, G., Laude, V., and Kadic, M., 2022, "3D Lightweight Mechanical Metamaterial With Nearly Isotropic Inelastic Large Deformation Response," J. Mech. Phys. Solids, **169**(12), p. 105057.

[23] Chen, X., Ji, Q., Martinez, J. A., Tan, H., Ulliac, G., Laude, V., and Kadic, M., 2022, "Closed Tubular Mechanical Metamaterial as Lightweight Load-Bearing Structure and Energy Absorber," J. Mech. Phys. Solids, **167**(10), p. 104957.

[24] Chen, X., Moughames, J., Ji, Q., Martínez, J. A., Tan, H., Adrar, S., Laforge, N., et al.et al., 2020, "Optimal Isotropic, Reusable Truss Lattice Material With Near-Zero Poisson's Ratio," Extrem. Mech. Lett., **41**(11), p. 101048.

[25] Iglesias Martínez, J. A., Groß, M. F., Chen, Y., Frenzel, T., Laude, V., Kadic, M., and Wegener, M., 2021, "Experimental Observation of Roton-Like Dispersion Relations in Metamaterials," Sci. Adv., **7**(49), p. 2189.

[26] Tan, X., Wang, L., Zhu, S., Chen, S., Wang, B., and Kadic, M., 2022, "A General Strategy for Performance Enhancement of Negative Stiffness Mechanical Metamaterials," Eur. J. Mech., **96**(11), p. 104702.

[27] Zhu, S., Wang, B., Chen, L., Tan, X., and Ma, L., 2022, "Enhance the Energy Dissipation Ability of Sleeve-Type Negative Stiffness Structures Via a Phase-Difference Mechanism," Int. J. Mech. Sci., **213**(1), p. 106803.

[28] Somers, P., Münchinger, A., Maruo, S., Moser, C., Xu, X., and Wegener, M., 2023, "The Physics of 3d Printing With Light," Nat. Rev. Phys., **6**(2), pp. 99–113.

[29] Wegener, M., 2023, "3D Laser Micro- and Nanoprinting: 10 Years of Progress," Laser 3D Manufacturing X, PC124120A (SPIE, 2023), San Francisco, CA, Jan. 31–Feb. 2.

[30] Porte, X., Dinc, N. U., Moughames, J., Panusa, G., Juliano, C., Kadic, M., Moser, C., Brunner, D., and Psaltis, D., 2021, "Direct (3 + 1) d Laser Writing of Graded-Index Optical Elements," Optica, **8**(10), pp. 1281–1287.

[31] Fan, J., Zhang, L., Wei, S., Zhang, Z., Choi, S. K., Song, B., and Shi, Y., 2021, "A Review of Additive Manufacturing of Metamaterials and Developing Trends," Mater. Today, **50**(11), pp. 303–328.

[32] Liu, S.-F., Hou, Z.-W., Lin, L., Li, Z., and Sun, H.-B., 2023, "3D Laser Nanoprinting of Functional Materials," Adv. Funct. Mater., **33**(39), p. 2211280.

[33] Baigarina, A., Shehab, E., and Ali, M. H., 2023, "Construction 3D Printing: A Critical Review and Future Research Directions," Prog. Addit. Manuf., **8**(6), pp. 1393–1421.

[34] Moughames, J., Porte, X., Larger, L., Jacquot, M., Kadic, M., and Brunner, D., 2020, "3d Printed Multimode-Splitters for Photonic Interconnects," Opt. Mater. Express, **10**(11), pp. 2952–2961.

[35] Hu, Z., Wei, Z., Wang, K., Chen, Y., Zhu, R., Huang, G., and Hu, G., 2023, "Engineering Zero Modes in Transformable Mechanical Metamaterials," Nat. Commun., **14**(1), p. 1266.

[36] Wang, L., Martínez, J. A., Ulliac, G., Wang, B., Laude, V., and Kadic, M., 2023, "Non-Reciprocal and Non-Newtonian Mechanical Metamaterials," Nat. Commun., **14**(1), p. 4778.

[37] Tan, X., Cao, B., Liu, W., Ji, C., Wang, B., and Li, S., 2024, "Odd Mechanical Metamaterials With Simultaneously Expanding or Contracting Under Both Compression and Tension," Thin Walled Struct., **203**(14), p. 112225.

[38] Janbaz, S., Narooei, K., Van Manen, T., and Zadpoor, A., 2020, "Strain Rate–Dependent Mechanical Metamaterials," Sci. Adv., **6**(25), p. eaba0616.

[39] Fang, X., Wen, J., Cheng, L., Yu, D., Zhang, H., and Gumbsch, P., 2022, "Programmable Gear-Based Mechanical Metamaterials," Nat. Mater., **21**(8), pp. 869–876.

[40] Milton, G. W., and Willis, J. R., 2007, "On Modifications of Newton's Second Law and Linear Continuum Elastodynamics," Proc. Royal Soc. A, **463**(2079), pp. 855–880.

[41] Liu, Z., Zhang, X., Mao, Y., Zhu, Y. Y., Yang, Z., Chan, C. T., and Sheng, P., 2000, "Locally Resonant Sonic Materials," Science, **289**(5485), pp. 1734–1736.

[42] Münchinger, A., Hsu, L.-Y., Fürniß, F., Blasco, E., and Wegener, M., 2022, "3D Optomechanical Metamaterials," Mater. Today, **59**(10), pp. 9–17.

[43] Meng, Z., Liu, M., Zhang, Y., and Chen, C. Q., 2020, "Multi-Step Deformation Mechanical Metamaterials," J. Mech. Phys. Solids, **144**(11), p. 104095.

[44] Liang, X., Fu, H., and Crosby, A. J., 2022, "Phase-Transforming Metamaterial With Magnetic Interactions," Proc. Natl. Acad. Sci. U.S.A., **119**(1), p. e2118161119.

[45] Ji, Q., Moughames, J., Chen, X., Fang, G., Huaroto, J. J., Laude, V., Martínez, J. A., et al., 2021, "4D Thermomechanical Metamaterials for Soft Microrobotics," Commun. Mater., **2**(1), p. 93.

[46] Farzaneh, A., Pawar, N., Portela, C. M., and Hopkins, J. B., 2022, "Sequential Metamaterials With Alternating Poisson's Ratios," Nat. Commun., **13**(1), p. 1041.

[47] Dudek, K. K., Iglesias Martínez, J. A., Ulliac, G., Hirsinger, L., Wang, L., Laude, V., and Kadic, M., 2023, "Micro-Scale Mechanical Metamaterial With a Controllable Transition in the Poisson's Ratio and Band Gap Formation," Adv. Mater., **35**(20), p. 2210993.

[48] Wang, L., Ulliac, G., Wang, B., Iglesias Martínez, J. A., Dudek, K. K., Laude, V., and Kadic, M., 2022, "3D Auxetic Metamaterials With Elastically-Stable Continuous Phase Transition," Adv. Sci., **9**(34), p. 2204721.

[49] Bertoldi, K., Reis, P. M., Willshaw, S., and Mullin, T., 2010, "Negative Poisson's Ratio Behavior Induced by an Elastic Instability," Adv. Mater., **22**(3), pp. 361–366.

[50] Babaee, S., Shim, J., Weaver, J. C., Chen, E. R., Patel, N., and Bertoldi, K., 2013, "3D Soft Metamaterials With Negative Poisson's Ratio," Adv. Mater., **25**(36), pp. 5044–5049.

[51] Tan, X., Martínez, J. A., Ulliac, G., Wang, B., Wu, L., Moughames, J., Raschetti, M., Laude, V., and Kadic, M., 2022, "Single-Step-Lithography Micro-Stepper Based on Frictional Contact and Chiral Metamaterial," Small, **18**(28), p. 2202128.

[52] Wang, Y., Li, L., Hofmann, D., Andrade, J. E., and Daraio, C., 2021, "Structured Fabrics With Tunable Mechanical Properties," Nature, **596**(7871), pp. 238–243.

[53] Lakes, R., 1987, "Foam Structures With a Negative Poisson's Ratio," Science, **235**(4792), pp. 1038–1040.
[54] Evans, K. E., and Alderson, A., 2000, "Auxetic Materials: Functional Materials and Structures From Lateral Thinking!," Adv. Mater., **12**(9), pp. 617–628.
[55] Wang, L., Tan, X., Zhu, S., Wang, B., Li, S., Zou, Y., and Chen, S., 2021, "Directional Instability-Driven Strain-Dependent 3D Auxetic Metamaterials," Int. J. Mech. Sci., **199**(6), p. 106408.
[56] Wang, L., Zhu, S., Wang, B., Tan, X., Zou, Y., Chen, S., and Li, S., 2021, "Latitude-and-Longitude-Inspired Three-Dimensional Auxetic Metamaterials," Extrem. Mech. Lett., **42**(1), p. 101142.
[57] Yang, H., Wang, B., and Ma, L., 2019, "Mechanical Properties of 3D Double-U Auxetic Structures," Int. J. Solids Struct., **180**(12), pp. 13–29.
[58] Gao, Y., Wei, X., Han, X., Zhou, Z., and Xiong, J., 2021, "Novel 3D Auxetic Lattice Structures Developed Based on the Rotating Rigid Mechanism," Int. J. Solids Struct., **233**(12), p. 111232.
[59] Setyawan, W., and Curtarolo, S., 2010, "High-Throughput Electronic Band Structure Calculations: Challenges and Tools," Comput. Mater. Sci., **49**(2), pp. 299–312.
[60] Ma, G., and Sheng, P., 2016, "Acoustic Metamaterials: From Local Resonances to Broad Horizons," Sci. Adv., **2**(2), p. e1501595.
[61] Cummer, S. A., Christensen, J., and Alù, A., 2016, "Controlling Sound With Acoustic Metamaterials," Nat. Rev. Mater., **1**(3), pp. 1–13.
[62] Christensen, J., Kadic, M., Kraft, O., and Wegener, M., 2015, "Vibrant Times for Mechanical Metamaterials," MRS Commun., **5**(3), pp. 453–462.
[63] Bauer, J., Kraus, J. A., Crook, C., Rimoli, J. J., and Valdevit, L., 2021, "Tensegrity Metamaterials: Toward Failure-Resistant Engineering Systems Through Delocalized Deformation," Adv. Mater., **33**(10), p. 2005647.
[64] Shan, S., Kang, S. H., Raney, J. R., Wang, P., Fang, L., Candido, F., Lewis, J. A., and Bertoldi, K., 2015, "Multistable Architected Materials for Trapping Elastic Strain Energy," Adv. Mater., **27**(29), pp. 4296–4301.